

Pseudogap and electronic structure of electron-doped Sr_2IrO_4

Alice Moutenet,^{1,2} Antoine Georges,^{2,3,1,4} and Michel Ferrero^{1,2}

¹Centre de Physique Théorique, École Polytechnique, CNRS, Université Paris-Saclay, 91128 Palaiseau, France

²Collège de France, 11 place Marcelin Berthelot, 75005 Paris, France

³Center for Computational Quantum Physics, Flatiron Institute, 162 Fifth Avenue, New York, NY 10010, USA

⁴Department of Quantum Matter Physics, University of Geneva,
24 Quai Ernest-Ansermet, 1211 Geneva 4, Switzerland

(Dated: January 29, 2018)

We present a theoretical investigation of the effects of correlations on the electronic structure of the Mott insulator Sr_2IrO_4 upon electron doping. A rapid collapse of the Mott gap upon doping is found, and the electronic structure displays a strong momentum-space differentiation at low doping level: The Fermi surface consists of pockets centered around $(\pi/2, \pi/2)$, while a pseudogap opens near $(\pi, 0)$. Its physical origin is shown to be related to short-range spin correlations. The pseudogap closes upon increasing doping, but a differentiated regime characterized by a modulation of the spectral intensity along the Fermi surface persists to higher doping levels. These results, obtained within the cellular dynamical mean-field theory framework, are discussed in comparison to recent photoemission experiments and an overall good agreement is found.

I. INTRODUCTION

Understanding the physical mechanism responsible for the pseudogap in cuprate superconductors, and its interplay with superconductivity, is still a central and very debated question in the field of strongly-correlated materials. In this respect, the Sr_2IrO_4 iridate is a very interesting playground as it closely resembles these materials. It is indeed isostructural to La_2CuO_4 ,¹ and its low-energy electronic structure is well described by a single half-filled band because of strong spin-orbit (SO) coupling as shown by electronic structure calculations in the Local Density Approximation (LDA).^{2,3} Angular Resolved PhotoEmission Spectroscopy (ARPES), optical spectroscopy, and resonant inelastic X-ray scattering experiments^{2,4-7} as well as scanning tunneling microscopy⁸ demonstrate that the ground-state of this material is a Mott insulator. This conclusion is also supported by electronic structure calculations taking into account electronic correlations.^{3,9} The similarity between the low-energy electronic structure of Sr_2IrO_4 and that of cuprates has led to the quest for superconductivity upon doping in this material.¹⁰⁻¹³

The electronic configuration of the Ir^{4+} ions is $\{\text{Xe}\}f^{14}5d^5$ and Sr_2IrO_4 crystallizes in the K_2NiF_4 tetragonal structure, as La_2CuO_4 or Sr_2RhO_4 .¹ The IrO_6 octahedra are rotated about the c -axis by ~ 11 deg., generating a doubled unit cell.¹⁴ The $5d^5$ electronic configuration would naively lead to a metallic state in a band theory approach. Sr_2RhO_4 , having an identical atomic arrangement with nearly the same lattice constants and bond angles, is indeed found to be a Fermi liquid metal.¹⁵ Sr_2IrO_4 however has a very strong SO coupling, a property which was shown to modify the electronic structure near the Fermi level in $5d$ systems.^{3,9,16-18} This compound then effectively reduces to a half-filled $j_{\text{eff}} = 1/2$ single band near the Fermi surface, a configuration which makes it prone to the opening of a Mott gap as a result of repulsive interactions.

As the non-interacting Fermi surface of this material is electron-like, the hole-doped regime of high-Tc cuprates is to be compared with the electron-doped one of Sr_2IrO_4 . Several experimental groups performed ARPES measurements

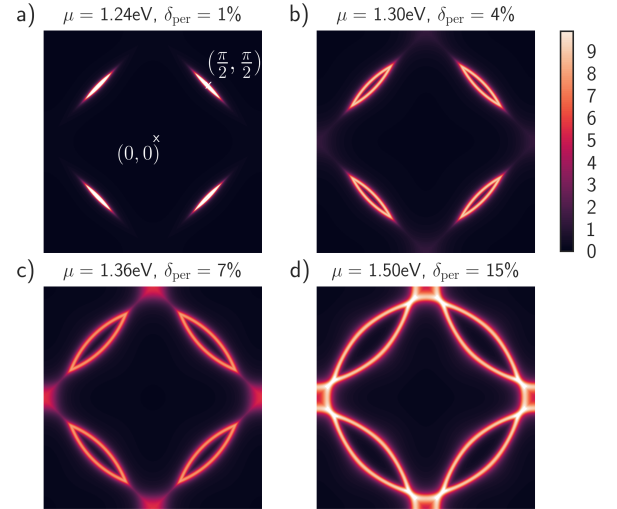


FIG. 1. Spectral intensity at the Fermi surface illustrating the evolution of the electronic structure upon increasing doping level, as described in the text. At low doping, the Fermi surface only consists in pockets near $(\pi/2, \pi/2)$ and a pseudogap is found near the antinodes. Results obtained within CDMFT and a periodized self-energy for $U = 2$ eV at $T = 58$ K (see text).

on Sr_2IrO_4 to investigate the doped compound further.^{5-7,19} Spectral intensity at the Fermi surface exhibits a strong momentum differentiation leading to the appearance of pockets in the ‘nodal’ region located around $(\pi/2, \pi/2)$,^{5,19} while the ARPES spectra in the ‘antinodal’ region around $(\pi, 0)$ are suggestive of a pseudogap.⁵ Note that the ‘nodal/antinodal’ terminology is inherited from the cuprate context and does not refer to the nodes of a superconducting gap - up to now no unambiguous evidence of superconductivity has been established.

In this article, we construct a theoretical model of the low-energy electronic structure of doped Sr_2IrO_4 , treating electronic correlation effects in the framework of cellular dynamical

cal mean-field theory (CDMFT).^{24,25} The Fermi surface spectral intensity maps displayed in Fig. 1 summarize key aspects of our results. Four successive doping regimes are found: The Mott insulating state (not displayed in Fig. 1) evolves into a metal with strong nodal-antinodal differentiation at low doping level. In this regime, the Fermi surface consists in pockets around $(\pi/2, \pi/2)$ (a-b), while the antinodal region displays a pseudogap, as shown below. Increasing doping further, spectral intensity appears near the antinodes with still a pronounced differentiation (c). A full Fermi surface, close to the uniform non-interacting one, is recovered at higher doping (d).

A previous theoretical study²⁰ addressed the issue of nodal-antinodal differentiation in this material, but the opening of the antinodal pseudogap and the associated spectral signatures could not be discussed due to the limitations of the slave-boson method used in that work.

This article is organized as follows. In Sec. II, we briefly summarize the tight-binding (TB) model of the electronic structure established in previous works and derive an effective model for the $j_{\text{eff}} = 1/2$ states. In Sec. III, we introduce correlations in this model and explain how to deal with these within the CDMFT scheme. We discuss results of such CDMFT calculations in Sec. IV and particularly the emergence of the four doping regimes sketched above. In order to restore translational symmetry which is broken in CDMFT, we introduce a periodization scheme for the self-energy in Sec. V. This allows for a calculation of the spectral intensities, which are found to be in good agreement with the existing ARPES measurements. We also discuss the spectral signatures of the antinodal pseudogap. In Sec. VI, we compute and discuss the quasiparticle band structure. Sec. VII is devoted to a discussion and concluding remarks.

II. TIGHT-BINDING MODEL

In this section, we describe the electronic band structure of Sr_2IrO_4 , derive an effective model for the $j_{\text{eff}} = 1/2$ states, and emphasize that the low-energy states can be described by a single band tight-binding model defined on a periodic lattice with a single atom per unit cell.

Our starting point is the tight-binding (TB) model introduced in Refs. 21 and 22 describing t_{2g} bands in the presence of a spin-orbit coupling. Because of the rotation of the IrO_6 octahedra around the c -axis, the Sr_2IrO_4 unit cell is composed of two inequivalent sites A and B . The tight-binding Hamiltonian is then written as

$$\mathcal{H}_0 = \sum_{\mathbf{k} \in \text{RBZ}} \psi_{\mathbf{k}}^\dagger H_0(\mathbf{k}) \psi_{\mathbf{k}}, \quad (1)$$

where the momentum sum is over the $\sqrt{2} \times \sqrt{2}$ reduced Brillouin zone and the components of $\psi_{\mathbf{k}}$ are the electron annihilation operators for all 12 orbitals in the unit cell $\{c_{\mathbf{k}\tau\alpha\sigma} | \tau = A, B; \alpha = d_{xy}, d_{yz}, d_{zx}; \sigma = \uparrow, \downarrow\}$. It is convenient to order the basis according to $(c_{A d_{xy} \uparrow}, c_{A d_{yz} \downarrow}, c_{A d_{zx} \downarrow}, [A \leftrightarrow B])$ followed by their time-reversed partners ($[\uparrow \leftrightarrow \downarrow]$). There is

no coupling between these two blocks as the system is time-reversal invariant and we can thus only consider the first half of the basis, taking into account that all bands are two-fold degenerate. The remaining 6×6 tight-binding matrix H_0 writes

$$H_0(\mathbf{k}) = \begin{pmatrix} O(\mathbf{k}) & P(\mathbf{k}) \\ P^\dagger(\mathbf{k}) & O(\mathbf{k}) \end{pmatrix}, \quad (2)$$

where P describes the hopping part of the Hamiltonian

$$P(\mathbf{k}) = e^{-i \frac{k_x + k_y}{2}} \begin{pmatrix} -4t_1(\mathbf{k}) & 0 & 0 \\ 0 & -2t_2(\mathbf{k}) & 0 \\ 0 & 0 & -2t_3(\mathbf{k}) \end{pmatrix}, \quad (3)$$

with $t_1(\mathbf{k}) = t_0 \cos \frac{k_x}{2} \cos \frac{k_y}{2}$, $t_2(\mathbf{k}) = t_0 \cos \frac{k_x + k_y}{2}$ and $t_3(\mathbf{k}) = t_0 \cos \frac{k_x - k_y}{2}$. Here $\mathbf{k} = (k_x, k_y)$ is expressed in terms of the reciprocal vectors forming the reduced Brillouin zone. O describes the on-site part of the Hamiltonian. It includes the spin-orbit coupling $\lambda \mathbf{L}_i \cdot \mathbf{S}_i$ and reads

$$O(\mathbf{k}) = \begin{pmatrix} \Delta_t + e_1(t_1(\mathbf{k})/t_0)^2 & \lambda/2 & -i\lambda/2 \\ \lambda/2 & 0 & -i\lambda/2 \\ i\lambda/2 & i\lambda/2 & 0 \end{pmatrix}, \quad (4)$$

where Δ_t is an on-site energy difference of the d_{xy} orbital relative to d_{yz} and d_{zx} , and λ is the spin-orbit coupling parameter. The additional term $e_1(t_1/t_0)^2$ accounts for the hybridization between d_{xy} and $d_{x^2-y^2}$.²¹ In the following we consider $\Delta_t = 0.15$ eV, $t_0 = 0.35$ eV, $e_1 = -1.5$ eV and $\lambda = 0.57$ eV. It has been shown that these values yield a band structure in good agreement with LDA+SO calculations.^{5,21}

We plot in Fig. 2 (upper panel) the six bands resulting from the diagonalization of $H_0(\mathbf{k})$ along the $(0, 0) - (\pi/2, \pi/2) - (\pi, 0) - (0, 0)$ path of the full Brillouin zone. When the eigenvalues are projected on the $j_{\text{eff}} = 1/2$ states

$$\left| j_{\text{eff}} = \frac{1}{2}, \pm \frac{1}{2} \right\rangle = \mp \frac{1}{\sqrt{3}} [|d_{xy}, \pm\rangle \pm (|d_{yz}, \mp\rangle \pm i|d_{zx}, \mp\rangle)], \quad (5)$$

it can be seen that the low-energy bands essentially have $j_{\text{eff}} = 1/2$ character, as highlighted in Refs 2, 5, 21, and 22. It is therefore natural to look for an effective reduced 2×2 Hamiltonian describing these states.

To do so, we rewrite H_0 in the basis $(|\frac{1}{2}, \frac{1}{2}\rangle_A, |\frac{1}{2}, \frac{1}{2}\rangle_B, |\frac{3}{2}, \frac{1}{2}\rangle_A, |\frac{3}{2}, \frac{1}{2}\rangle_B, |\frac{3}{2}, \frac{-3}{2}\rangle_A, |\frac{3}{2}, \frac{-3}{2}\rangle_B)$:

$$H_0(\mathbf{k}) = \begin{pmatrix} H_{1/2}(\mathbf{k}) & M(\mathbf{k}) \\ M^\dagger(\mathbf{k}) & H_{3/2}(\mathbf{k}) \end{pmatrix}, \quad (6)$$

where the exact expressions of $H_{1/2}$, M and $H_{3/2}$ are given in Appendix A. An effective Hamiltonian is then obtained by projecting H_0 onto the $j_{\text{eff}} = 1/2$ subspace:

$$H_{1/2}^{\text{eff}}(\mathbf{k}) = H_{1/2}(\mathbf{k}) + M(\mathbf{k}) [E \times \mathbf{1}_{4 \times 4} - H_{3/2}(\mathbf{k})]^{-1} M^\dagger(\mathbf{k}), \quad (7)$$

where $\mathbf{1}_{4 \times 4}$ is the 4×4 unit matrix and E an energy scale that is adjusted in order to best match the original band structure.

While it is difficult to have a compact expression for this reduced Hamiltonian, one can easily diagonalize $H_{1/2}^{\text{eff}}$ numerically for every \mathbf{k} point of interest. This is shown (red lines)

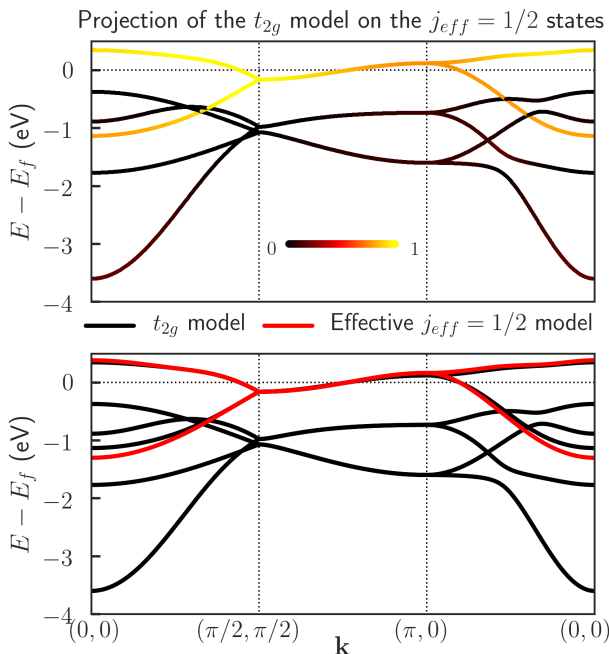


FIG. 2. *Upper panel:* Projection of the tight-binding model for the t_{2g} bands (Eq. (2)) on the $j_{\text{eff}} = 1/2$ states. The value of the projection ranges from 0 (black) to 1 (yellow). *Lower panel:* Comparison between the full t_{2g} model (black lines) and the effective $j_{\text{eff}} = 1/2$ model from Eq. (7) (red lines) with $E = 0$. On both panels, bands are plotted in reciprocal space, along the $(0, 0) - (\pi/2, \pi/2) - (\pi, 0) - (0, 0)$ path of the full Brillouin zone. $\Delta_t = 0.15$ eV, $t_0 = 0.35$ eV, $e_1 = -1.5$ eV and $\lambda = 0.57$ eV.

in Fig. 2 (lower panel) together with the complete t_{2g} band structure (black lines). The effective model appears to be in excellent agreement with the two low-energy bands exhibiting a $j_{\text{eff}} = 1/2$ character.

As mentioned earlier, the Sr_2IrO_4 crystal has a two-atom unit cell and we expressed the tight-binding models above in the reduced Brillouin zone in order to make contact with experiments. Let us however emphasize that all sites are actually equivalent from a purely electronic point of view in these models. An inspection of the band structure in the reduced Brillouin zone indeed reveals that it results from the folding of half as many bands defined over the full Brillouin zone. This can be seen e.g. from the degeneracy of the bands along the $(\pi/2, \pi/2) - (\pi, 0)$ path of the full Brillouin zone. As a result, the effective model in Eq. (7) can be written as a simple tight-binding model on a square lattice

$$\mathcal{H}_{1/2}^{\text{eff}} = \sum_{ij} t_{ij} c_i^\dagger c_j, \quad (8)$$

where the hopping amplitudes t_{ij} are shown as a function of the distance $|i - j|$ in Fig. 3 (upper panel). We see that one obtains a good approximation of the band structure by only keeping the nearest and next-nearest neighbor hopping terms (for an almost perfect agreement it is necessary to keep 8 hopping parameters). This yields the simple energy dispersion

$$\epsilon(\mathbf{k}) = \epsilon_0 + 2t(\cos k_x + \cos k_y) + 4t' \cos k_x \cos k_y, \quad (9)$$

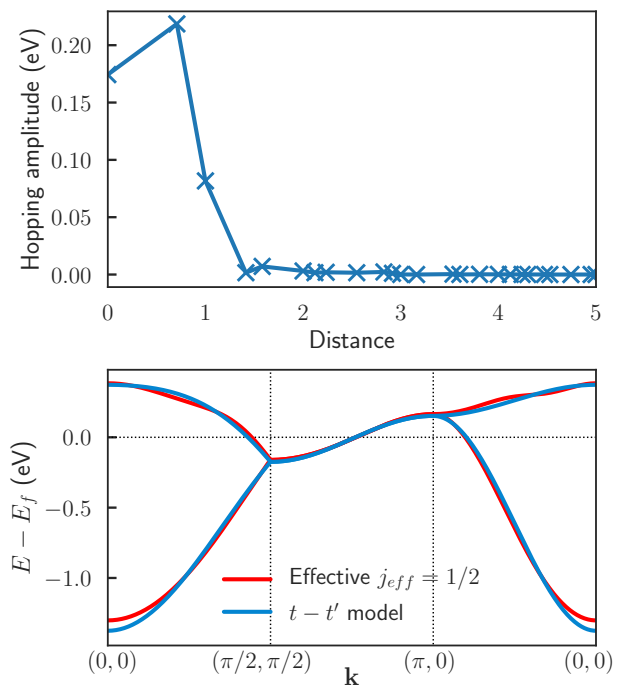


FIG. 3. *Upper panel:* Real-space hopping amplitudes of effective $j_{\text{eff}} = 1/2$ Hamiltonian the effective with respect to the distance (the inter-site distance is normalized to 1). *Lower panel:* Comparison between the effective $j_{\text{eff}} = 1/2$ bands (red) with $E = 0$ and the folded dispersion obtained by keeping only the nearest and next-nearest neighbor hopping terms ($t = -0.219$ eV, $t' = -0.082$ eV respectively). Bands are plotted in reciprocal space, along the $(0, 0) - (\pi/2, \pi/2) - (\pi, 0) - (0, 0)$ path of the full Brillouin zone. $\Delta_t = 0.15$ eV, $t_0 = 0.35$ eV, $e_1 = -1.5$ eV and $\lambda = 0.57$ eV.

where $\epsilon_0 = -0.174$ eV, $t = -0.219$ eV, $t' = -0.082$ eV and $\mathbf{k} = (k_x, k_y)$ is now expressed in the basis of the *full* Brillouin zone. The folding of this band in the reduced Brillouin zone is shown together with the effective $j_{\text{eff}} = 1/2$ band structure previously derived in Fig. 3 (lower panel). Let us mention that a similar tight-binding model was derived in Ref. 23 with the difference that the $d_{x^2-y^2}$ admixture was not included in their work.

In the following we use the effective Hamiltonian $\mathcal{H}_{1/2}^{\text{eff}}$ to describe the low-energy excitations of the system.

III. INTRODUCING CORRELATIONS

We model the effect of electronic correlations in Sr_2IrO_4 with a Hubbard Hamiltonian that introduces an energy cost for having two electrons on the same Ir atom

$$\mathcal{H} = \mathcal{H}_{1/2}^{\text{eff}} + U \sum_{i,\tau} n_{i\tau\uparrow} n_{i\tau\downarrow}, \quad (10)$$

where $n_{i\tau\sigma}$ is the occupation number on the $j_z = \sigma$ orbital of the Ir atom $\tau = A, B$ in the unit cell i . In the following we use $U = 2$ eV^{5,21} and temperature $T = 1/\beta = 1/200$ eV $\simeq 58$ K.

This model is studied using cellular dynamical mean-field theory^{24,25}: The original lattice Hamiltonian (10) is mapped on a two-site auxiliary cluster model embedded in a self-consistent medium. The self-energy of the cluster model $\Sigma_{\tau,\tau'}$ is used to construct an approximation of the lattice self-energy where only intra unit cell components are non-vanishing, i.e. $\Sigma_{i\tau,i\tau'}^{\text{latt}} = \Sigma_{\tau,\tau'}$. Note that the orbitals at sites A and B are electronically equivalent and therefore $\Sigma_{AA} = \Sigma_{BB}$ and $\Sigma_{AB} = \Sigma_{BA}$. We then have the following expression for the lattice Green's function

$$\hat{G}^{\text{latt}}(i\omega_n, \mathbf{k}) = \left\{ (i\omega_n + \mu)\mathbf{1} - H_{1/2}^{\text{eff}}(\mathbf{k}) - \hat{\Sigma}(i\omega_n) \right\}^{-1}, \quad (11)$$

where \mathbf{k} is defined in the reduced Brillouin zone and both \hat{G}^{latt} and $\hat{\Sigma}$ are 2×2 matrices associated with the two Ir atoms in the unit cell. The CDMFT self-consistency imposes that the cluster Green's function \hat{G} be the same as the unit cell Green's function of the lattice:

$$\hat{G}(i\omega_n) = \sum_{\mathbf{k} \in \text{RBZ}} \left\{ (i\omega_n + \mu)\mathbf{1} - H_{1/2}^{\text{eff}}(\mathbf{k}) - \hat{\Sigma}(i\omega_n) \right\}^{-1}. \quad (12)$$

We use a continuous-time quantum Monte Carlo (CT-HYB)²⁶⁻²⁹ impurity solver to find the solution of the two-site cluster model and the self-consistent equation (12) is solved iteratively.²⁵ More details are given in Appendix C. Codes necessary for the numerical calculations were developed using the TRIQS³⁰ library.

IV. THE FOUR DOPING REGIMES

We first investigate the cluster quantities \hat{G} and $\hat{\Sigma}$ obtained by solving the CDMFT equations. These quantities can be expressed in the basis $\{|\frac{1}{2}, \frac{1}{2}\rangle_A, |\frac{1}{2}, \frac{1}{2}\rangle_B\}$ of the $j_{\text{eff}} = 1/2$ orbitals on sites A and B . However, because A and B are electronically equivalent, it is convenient to work in the basis $\{|+\rangle, |-\rangle\}$ of even and odd combinations of the $j_{\text{eff}} = 1/2$ orbitals, defined by

$$|\pm\rangle = \frac{1}{\sqrt{2}} \left(\left| \frac{1}{2}, \frac{1}{2} \right\rangle_A \pm \left| \frac{1}{2}, \frac{1}{2} \right\rangle_B \right). \quad (13)$$

In this basis, both \hat{G} and $\hat{\Sigma}$ are diagonal (see Appendix C)

$$\hat{G} = \begin{pmatrix} G_+ & 0 \\ 0 & G_- \end{pmatrix} \quad \hat{\Sigma} = \begin{pmatrix} \Sigma_+ & 0 \\ 0 & \Sigma_- \end{pmatrix}. \quad (14)$$

As we will discuss later, G_{\pm} and Σ_{\pm} have a direct physical interpretation. The physics close to the node $(\pi/2, \pi/2)$ is indeed essentially controlled by G_- and Σ_- while the physics at the antinode $(\pi, 0)$ is controlled by G_+ and Σ_+ . The reason for this, anticipating on Sec. VI and Fig. 10, is that the nodal Fermi-surface pocket at $(\pi/2, \pi/2)$ is associated with the upper band (which has an antibonding/odd character) while the nodal states are associated with the lower bonding band with even character. The analysis of these quantities will reveal the existence of four distinct regimes upon doping: a Mott insulator phase, a pseudogap regime, a differentiation region and finally a uniform Fermi liquid state.

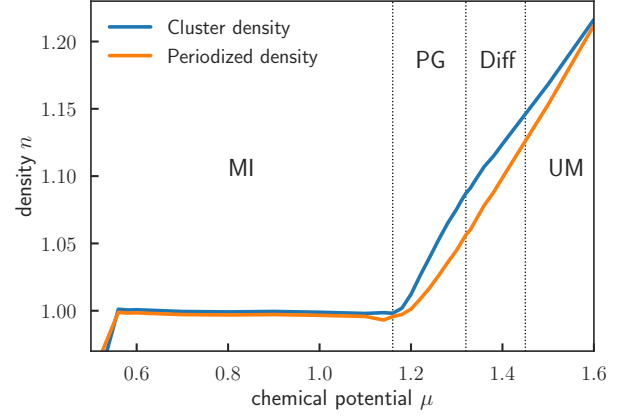


FIG. 4. Density of states as a function of the chemical potential μ . The cluster density is plotted in blue while the periodized one is plotted in orange. Dotted lines separate the four doping regimes: below $\mu = 1.16\text{eV}$ is the Mott insulating phase (MI), between $\mu = 1.16\text{eV}$ and $\mu = 1.32\text{eV}$ is the pseudogap regime (PG), between $\mu = 1.32\text{eV}$ and $\mu = 1.45\text{eV}$ is the differentiation region (Diff), and above $\mu = 1.45\text{eV}$ is the uniform metal (UM). Results obtained with a 2-site CDMFT calculation for $U = 2\text{ eV}$, $T = 58\text{ K}$.

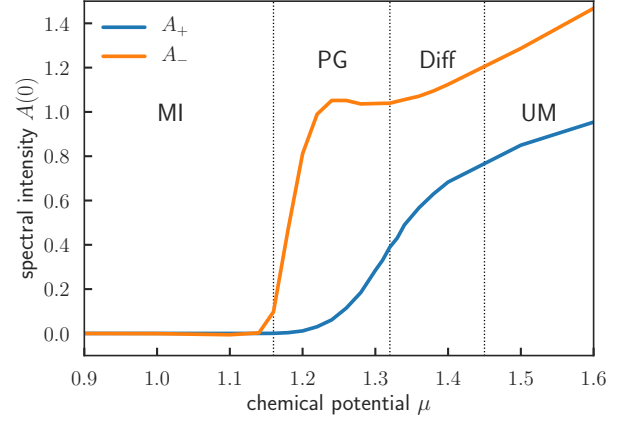


FIG. 5. Spectral intensity at the Fermi level $A(0)$ as a function of the chemical potential μ . The even (odd) contribution is plotted in blue (orange). Dotted lines separate the four doping regimes (see Fig. 4). Results obtained with a 2-site CDMFT calculation for $U = 2\text{ eV}$, $T = 58\text{ K}$.

The electronic density n is shown as a function of the chemical potential μ in Fig. 4 (blue curve). It displays a clear plateau at $n = 1$ for μ between 0.56eV and 1.16eV , confirming that the system is a Mott insulator at half-filling.^{2,3,9} The width of the plateau $\simeq 0.6\text{eV}$ is consistent with the recent experiment of Ref. 6.

In Fig. 5 and 6 are displayed the spectral intensities $A_{\pm}(\omega = 0)$ at the Fermi level as well as the zero-frequency self-energies $\Sigma_{\pm}(\omega = 0)$ as a function of the chemical potential μ . These quantities are obtained by extrapolating to zero

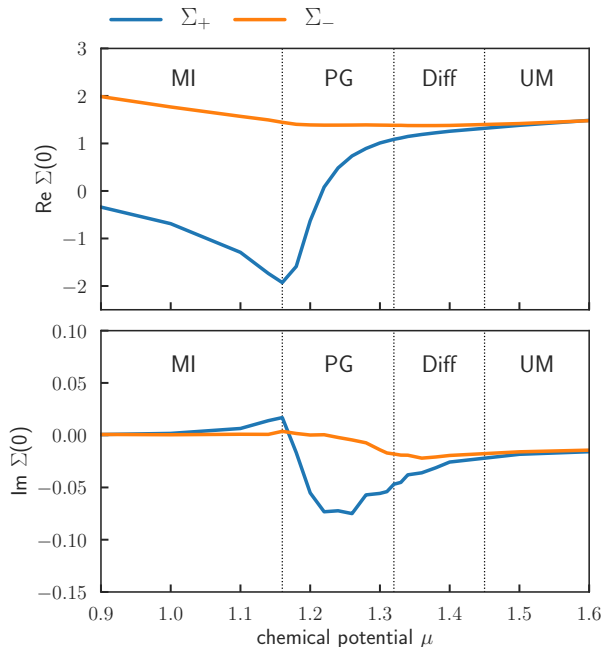


FIG. 6. Extrapolation at zero frequency of the real part (*upper panel*) and of the imaginary part (*lower panel*) of the self-energy $\Sigma(i\omega_n)$ as a function of the chemical potential μ . The even (odd) contribution is plotted in blue (orange). Dotted lines separate the four doping regimes (see Fig. 4). Results obtained with a 2-site CDMFT calculation for $U = 2$ eV, $T = 58$ K.

Matsubara frequencies results obtained by Monte Carlo:

$$A_{\pm}(0) = -\frac{1}{\pi} \lim_{i\omega_n \rightarrow 0} \text{Im} G_{\pm}(i\omega_n), \quad (15)$$

$$\Sigma_{\pm}(0) = \lim_{i\omega_n \rightarrow 0} \Sigma_{\pm}(i\omega_n). \quad (16)$$

For completeness, we have included plots of the Matsubara frequency Green's functions and self-energies for several chemical potentials in Appendix B.

These results allow to identify four distinct doping regimes. For chemical potentials smaller than $\mu = 1.16$ eV, the system is in a Mott insulating regime and both the even (+) and odd (-) components of the spectral intensity at the Fermi level are zero, $A_{\pm}(0) = 0$ (also both Matsubara Green's functions $G_{\pm}(i\omega_n)$ have clear insulating character, see Appendix B). This is compatible with the location of the Mott plateau in Fig. 4. Correlation effects are especially visible in the very different values of the real parts of the self-energies while both imaginary parts vanish. As a result, the effective low-energy band structure is split by the real parts of the self-energy in Eq. (12) and no excitations exist at $\omega = 0$. More precisely, the quasiparticle equation

$$\det \left\{ (\omega + \mu) \mathbf{1} - H_{1/2}^{\text{eff}}(\mathbf{k}) - \hat{\Sigma}(\omega) \right\} = 0 \quad (17)$$

has no solutions at $\omega = 0$ for all values of \mathbf{k} .

When μ lies between 1.16 eV and 1.32 eV, we enter a *pseudogap* regime. The even component of the Green's function,

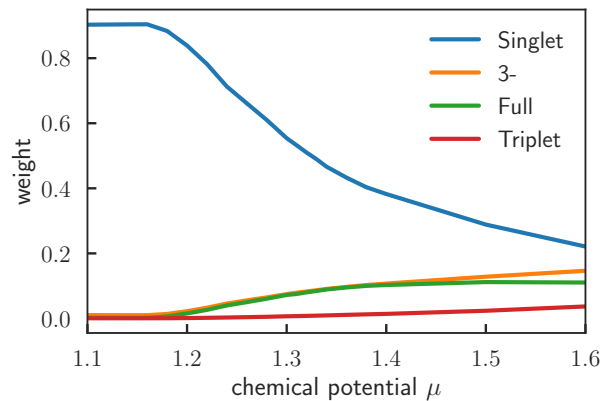


FIG. 7. Statistical weights of states dominating the Monte Carlo sampling on the dimer cluster of the CDMFT approach, as a function of the chemical potential μ . The dominant state is found to be the 2-electron inter-site singlet (blue). As doping level is increased, the three-electrons odd parity state catches up, denoted here as 3- (orange) - as well as the fully occupied state (green), while the 2-electron triplet state (red) has a smaller weight. Other contributions are negligible.

that provides a coarse-grained picture of the physics close to the antinode $\mathbf{k} = (\pi, 0)$, maintains its insulating character ($A_+(0) = 0$) while the odd component, describing the nodal region close to $\mathbf{k} = (\pi/2, \pi/2)$, becomes metallic ($A_-(0) \neq 0$). This describes a metal that only has coherent quasiparticles close to the node. Antinodal particles are suppressed by lifetime effects, as can be seen from the more negative imaginary part of the even self-energy $\text{Im}\Sigma_+(0)$ reaching -0.1 eV in Fig. 6 while $\text{Im}\Sigma_-(0)$ remains very small. We show below that the spectral function exhibits a pseudogap at $\mathbf{k} = (\pi, 0)$ in this region. This regime is very reminiscent of the pseudogap region of cuprate superconductors.

As the electron doping is further increased, for $1.32 \leq \mu \leq 1.45$ eV, spectral weight starts appearing in $A_+(0)$, an indication that quasiparticles start forming at the antinode as well. However, there are still visible differences between the even and odd components of the self-energies (see also Appendix B). The regime is therefore characterized by a visible \mathbf{k} -space differentiation where lifetime effects are stronger at the antinode than at the node ($\text{Im}\Sigma_+(0) < \text{Im}\Sigma_-(0)$) but do not completely destroy quasiparticles.

Eventually, for μ above 1.45 eV, a uniform metallic regime settles where both self-energies are identical and \mathbf{k} -space differentiation has disappeared. This regime would be well described by a single-site DMFT calculation.

It should be emphasized that boundaries delimiting these different regimes correspond to crossovers and hence are defined here in a qualitative manner.

The physical mechanism responsible for the formation of the pseudogap and the strong nodal-antinodal dichotomy observed at low doping can be revealed by studying the many-body states associated with the 2-site cluster. Calculating these states' histogram, we identify those that contribute most to the stochastic sampling within the CT-HYB quantum im-

purity solver. This is shown in Fig. 7, from which it is clear that the system is dominated by the intra-dimer singlet state at low doping levels. This is a strong indication that physics in this regime is governed by the formation of short-range anti-ferromagnetic correlations between neighboring sites.

V. FERMI SURFACE AND PSEUDOGAP

We now turn to the study of the fermiology of the system. Within CDMFT, the lattice Green's function given by Eq. (11) breaks translational symmetry,²⁴ hence making a direct comparison to momentum-resolved ARPES experiments difficult. The reason for the symmetry breaking is the lattice self-energy in CDMFT only having components inside a unit cell but not between different unit cells. A natural way to restore the translational symmetry is to *periodize* the self-energy by propagating the intersite contribution Σ_{AB} over all links on the lattice. However an artifact of this periodization scheme is that it prevents the formation of a Mott insulator and gives a wrong description of the low-doping physics (see Appendix D for more details). We therefore design a different periodization that yields much more physical results and preserves the existence of the Mott insulator. In this scheme, the lattice self-energy is given by

$$\tilde{\Sigma}^{\text{latt}}(i\omega_n, \mathbf{k}) = \begin{pmatrix} \Sigma_{AA} & \Sigma_{AB} \times e^{-i\frac{k_1+k_2}{2}} \\ \Sigma_{AB} \times e^{i\frac{k_1+k_2}{2}} & \Sigma_{AA} \end{pmatrix}, \quad (18)$$

where $\mathbf{k} = (k_1, k_2)$ is expressed in the reduced Brillouin zone. With this self-energy, we then define a periodized lattice Green's function \tilde{G}^{latt} according to

$$\tilde{G}^{\text{latt}}(i\omega_n, \mathbf{k}) = \left\{ i\omega_n + \mu - H_{1/2}^{\text{eff}}(\mathbf{k}) - \tilde{\Sigma}^{\text{latt}}(i\omega_n, \mathbf{k}) \right\}^{-1}. \quad (19)$$

This Green's function preserves all the symmetries of the lattice and will be the basis of our analysis below.

As a consistency check we first compute in Fig. 4 the electronic density n as a function of μ obtained from \tilde{G} (orange curve). Comparing it to the cluster density (blue curve) discussed in Sec. IV, we see that plateaus at $n = 1$ match well, confirming the existence of a Mott insulator within our periodization scheme. However, the periodized density generally has a slightly lower values compared to the cluster density for a given chemical potential. In the following, we discuss our results for specific values of μ and thus indicate two corresponding values of the electron doping: the cluster and the periodized one (resp. δ_{cluster} and δ_{per}).

We plot in Fig. 1 the spectral intensity at the Fermi surface for four values of the chemical potential. At small doping levels, for $\mu \leq 1.30\text{eV}$, nodal pockets with coherent quasiparticles develop while the antinodal intensity is completely suppressed. For these values of μ , we are in the pseudogap regime discussed above. A closer inspection of the spectral function at $\mathbf{k} = (\pi, 0)$ for $\mu = 1.30\text{eV}$ indeed confirms the presence of a clear pseudogap: Fig. 8 shows the leading edge of the spectrum being shifted away from zero energy. As dis-

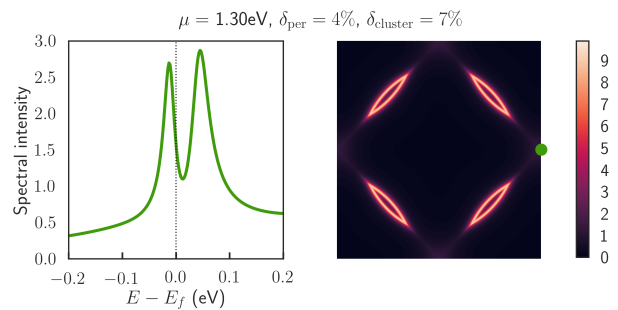


FIG. 8. *Left panel:* Spectral intensity $\text{Tr}A(\omega, \mathbf{k}_{\text{AN}})$ (Energy Distribution Curve - EDC) at the antinode $\mathbf{k}_{\text{AN}} = (\pi, 0)$ for $\mu = 1.3\text{ eV}$. *Right panel:* Spectral intensity at the Fermi surface with a periodized self-energy for the same μ . $U = 2\text{ eV}$, $T = 58\text{ K}$.

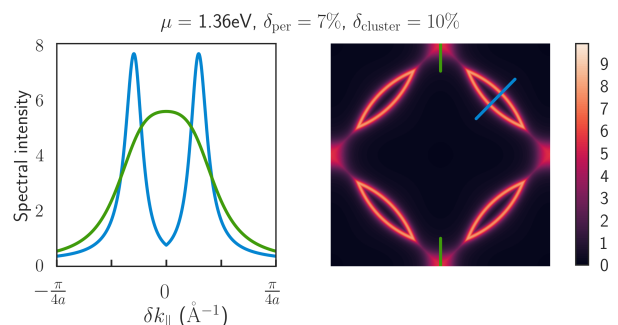


FIG. 9. *Left panel:* Spectral intensity at the Fermi surface $\text{Tr}A(\omega = 0, \mathbf{k})$ (Momentum Distribution Curve - MDC) for $\mu = 1.36\text{ eV}$ taken along the nodal (blue) and the antinodal (green) directions. Corresponding cuts are shown with the same color code on the right panel. *Right panel:* Spectral intensity at the Fermi surface with a periodized self-energy for the same μ . $U = 2\text{ eV}$, $T = 58\text{ K}$.

cussed above, we attribute its formation to short-range anti-ferromagnetic correlations (manifested here as the dominance of inter-site singlet dimer formation in our cluster, as revealed by the histogram of states).

As the electron doping is increased, the $(\pi/2, \pi/2)$ pockets grow and spectral intensity starts to appear around $(\pi, 0)$, see panel (c) of Fig. 1, leading to an extension of the Fermi surface over the Brillouin zone. Quasiparticles are however far more incoherent and broader at the antinode, as can be seen from momentum cuts across the node or the antinode (Fig. 9). While sharp coherent quasiparticles are found at the node, those at the antinode display a lower spectral intensity that is broadened over a greater region of \mathbf{k} -space. This corresponds to the momentum-differentiation regime introduced above.

At larger doping, the self-energy becomes finally uniform and the resulting Fermi surface displays coherent quasiparticles both at the node and the antinode, as shown in the panel (d) of Fig. 1.

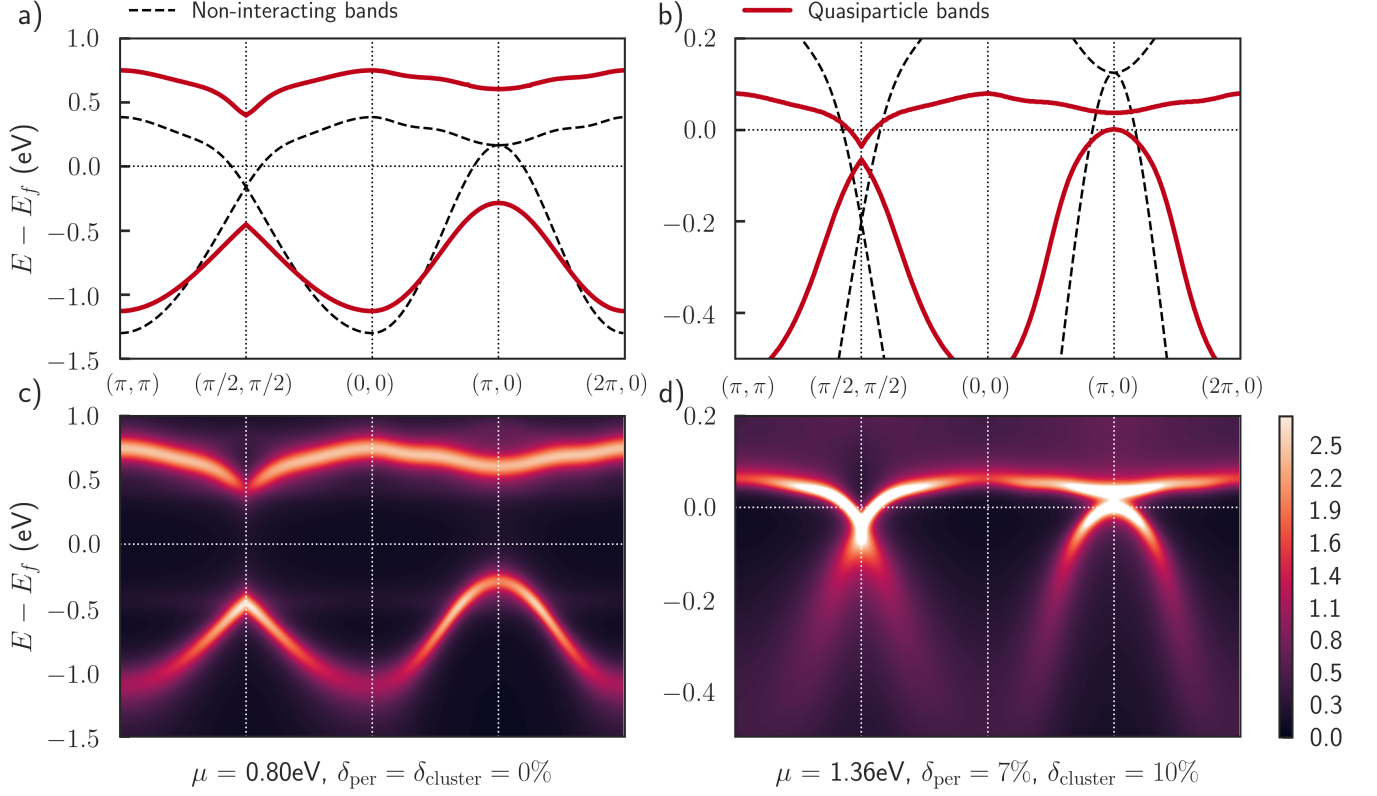


FIG. 10. Band dispersion of the insulating (a-c), $\mu = 0.8\text{eV}$, and doped (b-d), $\mu = 1.36\text{eV}$, Sr_2IrO_4 . Periodized self-energies are analytically continued from Padé approximants. *Upper panels:* Comparison between the non-interacting bands obtained from the TB + SO Hamiltonian $H_{1/2}^{\text{eff}}$ (dashed lines) and the quasiparticle bands. *Lower panels:* Spectral intensities, generalizing Fig. 1 away from the Fermi surface. All panels follow the $(\pi, \pi) - (\pi/2, \pi/2) - (0, 0) - (\pi, 0) - (2\pi, 0)$ path in the full Brillouin zone. $U = 2\text{ eV}$, $T = 58\text{ K}$.

VI. ELECTRONIC BAND STRUCTURE

We now turn to an analysis of the dispersion of quasiparticle bands in Sr_2IrO_4 . This requires to analytically continue our imaginary-frequency data to the real axis. We use Padé approximants³¹ to find $\tilde{\Sigma}^{\text{latt}}(\omega, \mathbf{k})$ from the knowledge of the periodized lattice self-energy $\tilde{\Sigma}^{\text{latt}}(i\omega_n, \mathbf{k})$. The resulting band structure is shown in Fig. 10 where we compare the insulating state at $\mu = 0.8\text{eV}$ (left panels) and the electron doped state at $\mu = 1.36\text{eV}$, $\delta_{\text{per}} = 7\%$, $\delta_{\text{cluster}} = 10\%$ (right panels). On the upper panels, we show the non-interacting bands obtained by diagonalizing the TB + SO Hamiltonian $H_{1/2}^{\text{eff}}$ (dashed lines) and the quasiparticle bands obtained from the solutions of

$$\det \left\{ (\omega + \mu)\mathbf{1} - H_{1/2}^{\text{eff}}(\mathbf{k}) - \tilde{\Sigma}^{\text{latt}}(\omega, \mathbf{k}) \right\} = 0. \quad (20)$$

Bands are plotted along the $(\pi, \pi) - (\pi/2, \pi/2) - (0, 0) - (\pi, 0) - (2\pi, 0)$ path of the full Brillouin zone. Lower panels display the corresponding total spectral intensity $\text{Tr}\hat{A}(\omega, \mathbf{k})$.

In the insulating region, the Mott gap is clearly visible. The band structure indicates that correlation effects have split the original non-interacting bands. This is compatible with the observation that, at $\mu = 0.8\text{eV}$, the cluster self-energies take

very different values $\text{Re}\Sigma_+(0) \neq \text{Re}\Sigma_-(0)$. Lifetime effects are also not very strong and the bands are fairly coherent, consistent with the fact that $\text{Im}\Sigma_{\pm}(0) \simeq 0$. The top of the lower band is located at $\simeq -0.4\text{ eV}$ at the node and at $\simeq -0.2\text{ eV}$ at the antinode. There is a direct gap to the unoccupied states of the order of 0.8 eV at $\mathbf{k} = (\pi/2, \pi/2)$, while the smallest overall gap is indirect and of order 0.6 eV . Note that the latter value is consistent with the width of the Mott plateau in Fig. 4.

As we move to the doped region, the Mott gap first closes at the nodal point $\mathbf{k} = (\pi/2, \pi/2)$ and the quasiparticle bands merge. The crossing of the upper band at two points close to $(\pi/2, \pi/2)$ is a signature of the pocket seen in the previous spectral intensities. Around these points, a clear renormalization of the Fermi velocities by a factor $1/4$ is visible as compared to the non-interacting bands. For $\mu = 1.36\text{eV}$ there is still a gap between the bands at $\mathbf{k} = (\pi, 0)$ but the lower band just reaches the Fermi level yielding some antinodal spectral weight. It is interesting to note that the correlation effects are much stronger on the lower band than on the upper band. Quasiparticles are then better defined at $(\pi/2, \pi/2)$ (they correspond to a crossing of the upper band) than at $(\pi, 0)$ where they are associated with the lower band. This is explained by the fact that the physics of the lower band is mainly controlled by the cluster Σ_+ , while the upper band is controlled by Σ_- . As a result, the larger negative imaginary part of Σ_+

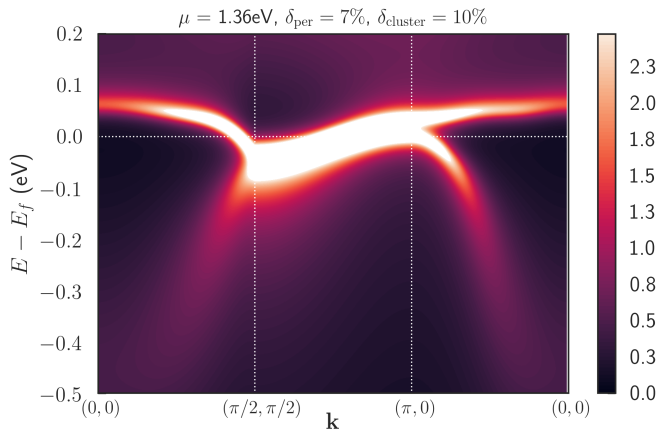


FIG. 11. Spectral intensity of the doped compound ($\mu = 1.36\text{eV}$) along the degenerate path $(0, 0) - (\pi/2, \pi/2) - (\pi, 0) - (0, 0)$ in the full Brillouin zone. Periodized self-energies are analytically continued from Padé approximants. $U = 2\text{ eV}$, $T = 58\text{ K}$.

(see Fig. 6) induces stronger lifetime effects at the antinode, while the smaller imaginary part of Σ_- maintains coherent quasiparticles at the node.

We finally display in Fig. 11 a spectral intensity map along the $(\pi/2, \pi, 2) - (\pi, 0)$ Brillouin zone path, which corresponds to the path along which the non-interacting bands are degenerate. ARPES data along this path have not appeared in print to our knowledge, and our results could be useful in the context of future analysis of ARPES experiments.

VII. DISCUSSION AND CONCLUSIONS

Finally, we discuss the comparison of our results with ARPES and other experiments on doped Sr_2IrO_4 .

Overall, there is excellent qualitative agreement. Comparing panels (a) and (b) of Fig. 10, a clear ‘collapse’ of the Mott gap is found upon doping the insulator (i.e the two bands become much closer to each other). This effect was reported in ARPES experiments:^{5,6} It is clearly apparent for example in Fig.2 (g-h) of Ref. 5 in which the top of the band at $(\pi/2, \pi/2)$ moves from about -0.4 eV to about -0.1 eV (band crossing) upon doping. In fact, the location of the top of the band at the ‘node’ (-0.4 eV) and ‘antinode’ (-0.2 eV) are in good quantitative agreement with the values reported in Ref. 5. The rather round and spread behavior of the band at the node quite agrees with the experiments even if the nodal part does not appear to be as narrow as it is observed.

The ‘nodal-antinodal’ differentiation and formation of a pseudogap near the ‘antinode’ is also consistent with the experimental observations.^{5,19} Here, we have shown that the

physical origin of the pseudogap is indeed the same than in cuprate superconductors, namely short-range spin correlations (see e.g. Refs. 32 and 33 for recent theoretical studies).

The value of the interaction parameter $U = 2\text{ eV}$ for which we chose to perform our calculations should also be discussed in the context of experimental measurements, especially of experimental determinations of the Mott gap. With this value, we find a Mott gap which is indirect and of order $\sim 0.6\text{ eV}$ - corresponding to the transition between the top of the lower Hubbard band at $(\pi, 0)$ and the bottom of the upper Hubbard band at $(\pi/2, \pi/2)$ in Fig. 10(a), and also to the width of the Mott plateau in Fig. 4. The value of the optical gap would be slightly larger. In Ref. 6, Sr_2IrO_4 was studied under both hole (Rh) and electron (La) doping, allowing for a determination of a Mott gap of order 0.7 eV , in rather good agreement with the present work. Optical spectroscopy measurements (see e.g Fig.4 in Ref. 2) do reveal a sharp increase of absorption in that frequency range, but a rather slow onset of the optical conductivity is observed with spectral weight below this scale, possibly suggesting a significantly smaller value of the actual gap (although a precise determination is difficult). This suggests that the value of U used in the present work may be a bit too large. Accordingly, we note that the Fermi surface renormalizations obtained above appear to be somewhat larger than the values reported in Ref. 5.

An ab-initio determination of the screened U appropriate for the low-energy model used here, as well as a more systematic study of this model as a function of U would be desirable in future work. In connection with the latter, a study of the possible superconducting instability as a function of U can be performed within cluster extensions of DMFT (CDMFT or DCA) for the present model and would shed light on the elusive superconductivity of doped Sr_2IrO_4 .

ACKNOWLEDGMENTS

We are grateful to Felix Baumberger, Alberto de la Torre, Sara Ricco and Anna Tamai for sharing with us their experimental results and for numerous discussions. We also acknowledge discussions with Luca Perfetti, Véronique Brouet, Dirk van der Marel, Nimrod Bachar, Silke Biermann, and thank the CPHT computer support team for their help. This work has been supported by the European Research Council grant ERC-319286-QMAC and the Swiss National Science Foundation (NCCR MARVEL). The Flatiron Institute is supported by the Simons Foundation.

Appendix A: Expression of H_0 in the j basis

Labeling $l(\mathbf{k}) = e^{-i\frac{k_x + k_y}{2}}$, we have

$$H_{1/2}(\mathbf{k}) = \begin{pmatrix} \frac{1}{3} \left[\Delta_t + e_1 \left(\frac{t_1(\mathbf{k})}{t_0} \right)^2 \right] + \lambda & -\frac{8}{3} l(\mathbf{k}) t_1(\mathbf{k}) \\ -\frac{8}{3} l^\dagger(\mathbf{k}) t_1(\mathbf{k}) & \frac{1}{3} \left[\Delta_t + e_1 \left(\frac{t_1(\mathbf{k})}{t_0} \right)^2 \right] + \lambda \end{pmatrix}, \quad (\text{A1})$$

and

$$M^\dagger(\mathbf{k}) = \begin{pmatrix} -\frac{\sqrt{2}}{3} \left[\Delta_t + e_1 \left(\frac{t_1(\mathbf{k})}{t_0} \right)^2 \right] & \frac{2\sqrt{2}}{3} l(\mathbf{k}) t_1(\mathbf{k}) \\ \frac{2\sqrt{2}}{3} l^\dagger(\mathbf{k}) t_1(\mathbf{k}) & -\frac{\sqrt{2}}{3} \left[\Delta_t + e_1 \left(\frac{t_1(\mathbf{k})}{t_0} \right)^2 \right] \\ 0 & \frac{2}{\sqrt{6}} l(\mathbf{k}) (t_2(\mathbf{k}) - t_3(\mathbf{k})) \\ \frac{2}{\sqrt{6}} l^\dagger(\mathbf{k}) (t_2(\mathbf{k}) - t_3(\mathbf{k})) & 0 \end{pmatrix}, \quad (\text{A2})$$

and

$$H_{3/2}(\mathbf{k}) = \begin{pmatrix} \frac{2}{3} \left[\Delta_t + e_1 \left(\frac{t_1(\mathbf{k})}{t_0} \right)^2 \right] - \frac{\lambda}{2} & -\frac{10}{3} l(\mathbf{k}) t_1(\mathbf{k}) & 0 & \frac{l(\mathbf{k})}{\sqrt{3}} (t_2(\mathbf{k}) - t_3(\mathbf{k})) \\ -\frac{10}{3} l^\dagger(\mathbf{k}) t_1(\mathbf{k}) & \frac{2}{3} \left[\Delta_t + e_1 \left(\frac{t_1(\mathbf{k})}{t_0} \right)^2 \right] - \frac{\lambda}{2} & \frac{l^\dagger(\mathbf{k})}{\sqrt{3}} (t_2(\mathbf{k}) - t_3(\mathbf{k})) & 0 \\ 0 & \frac{l(\mathbf{k})}{\sqrt{3}} (t_2(\mathbf{k}) - t_3(\mathbf{k})) & -\frac{\lambda}{2} & -2l(\mathbf{k}) t_1(\mathbf{k}) \\ \frac{l^\dagger(\mathbf{k})}{\sqrt{3}} (t_2(\mathbf{k}) - t_3(\mathbf{k})) & 0 & -2l^\dagger(\mathbf{k}) t_1(\mathbf{k}) & -\frac{\lambda}{2} \end{pmatrix}. \quad (\text{A3})$$

Appendix B: Green's functions and self-energy in the four doping regimes

In Fig. 12, we show the Matsubara frequency Green's functions and self-energies in the four doping regimes discussed in the main text. These regimes are here associated with four different values of the chemical potential corresponding to the four rows of the figure.

For $\mu = 1\text{eV}$ the system is a Mott insulator, as can be seen from the insulating character of the two components of the Green's function G_\pm . Let us note that the real parts of the self-energies are very different, which is responsible for the opening of the Mott gap (see main text). Increasing the doping, we enter a pseudogap phase. At $\mu = 1.2\text{eV}$, the even component of the Green's function has an insulating behavior while the odd one is metallic. At $\mu = 1.34\text{eV}$, the system is in a differentiate regime. Both components of the Green's function are now metallic but the self-energies are still quite differentiated. Going to even larger dopings we finally reach the uniform Fermi liquid state. Hence at $\mu = 1.5\text{eV}$, we see that G_+ and G_- are both metallic and that the self-energies tend to be identical.

Appendix C: Solving CDMFT equations

In order to solve the CDMFT equations, it is convenient to work in the \pm basis introduced in Eq. (13). In this basis, the lattice Green's function is

$$\hat{G}_\pm^{\text{latt}}(i\omega_n, \mathbf{k}) = \left\{ (i\omega_n + \mu) \mathbf{1} - H_\pm^{\text{eff}}(\mathbf{k}) - \hat{\Sigma}_\pm(i\omega_n) \right\}^{-1}, \quad (\text{C1})$$

where $H_\pm^{\text{eff}}(\mathbf{k})$ is the effective $j_{\text{eff}} = 1/2$ Hamiltonian expressed in the \pm basis and the cluster self-energy is diagonal because A and B sites are electronically equivalent

$$\hat{\Sigma}_\pm(i\omega_n) = \begin{pmatrix} \Sigma_+(i\omega_n) & 0 \\ 0 & \Sigma_-(i\omega_n) \end{pmatrix}. \quad (\text{C2})$$

Note that for a given \mathbf{k} point, $\hat{G}_\pm^{\text{latt}}(i\omega_n, \mathbf{k})$ is not diagonal. One can however show that, for a generic 2×2 diagonal matrix \mathcal{M} ,

$$\sum_{\mathbf{k} \in \text{RBZ}} [H_\pm^{\text{eff}}(\mathbf{k}) + \mathcal{M}]^{-1} \quad (\text{C3})$$

is a diagonal matrix too. As a result, the CDMFT self-consistency Eq. (12) becomes diagonal and reads

$$\hat{G}_\pm(i\omega_n) = \sum_{\mathbf{k} \in \text{RBZ}} \left\{ (i\omega_n + \mu) \mathbf{1} - H_\pm^{\text{eff}}(\mathbf{k}) - \hat{\Sigma}_\pm(i\omega_n) \right\}^{-1}, \quad (\text{C4})$$

where both cluster quantities \hat{G}_\pm and $\hat{\Sigma}_\pm$ are diagonal. This equation is solved iteratively in the following way: At the iteration step n , the quantum impurity model is described by a non-interacting Green's function $G_{0,\pm}^{(n)}$ and a local interaction Hamiltonian that has the following expression in the \pm basis

$$\mathcal{H}^{\text{int}} = \frac{U}{2} \sum_{s=\pm} (n_{s\uparrow} n_{s\downarrow} + n_{s\uparrow} n_{\bar{s}\downarrow} + c_{s\uparrow}^\dagger c_{s\downarrow}^\dagger c_{\bar{s}\downarrow} c_{\bar{s}\uparrow} + c_{s\uparrow}^\dagger c_{\bar{s}\downarrow}^\dagger c_{s\downarrow} c_{\bar{s}\uparrow}). \quad (\text{C5})$$

This cluster model is solved using the CT-HYB quantum impurity solver. This solver directly works in the \pm basis.

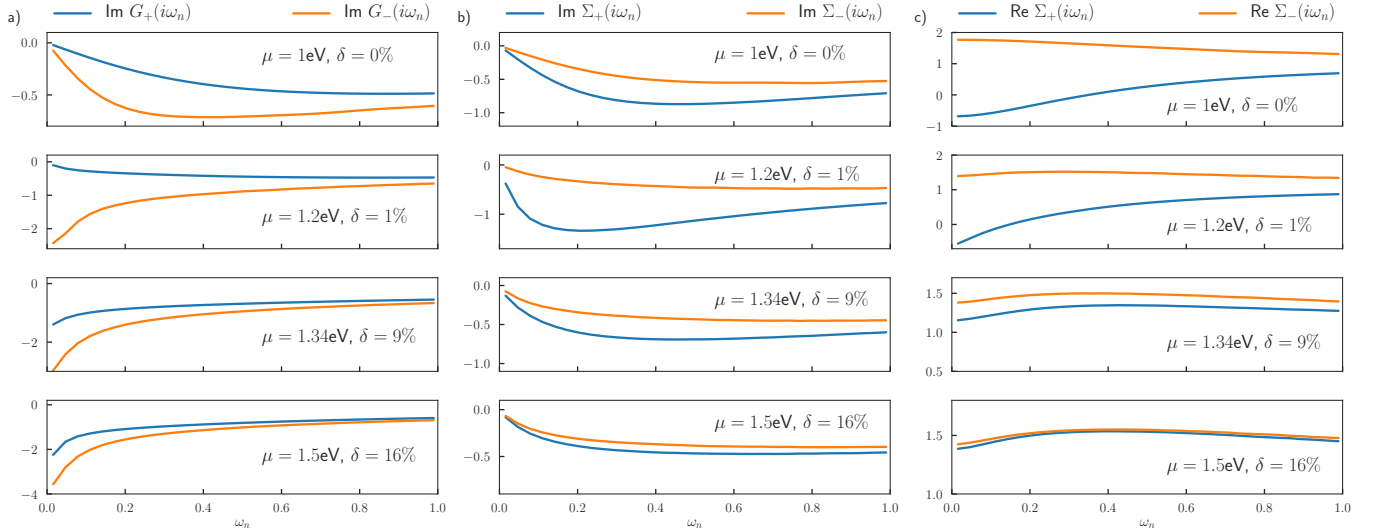


FIG. 12. Evolution in the even - odd basis of a) the imaginary part of the Green's function $G_{\pm}(i\omega_n)$, b) the real part of the self-energy $\Sigma_{\pm}(i\omega_n)$, c) the imaginary part of $\Sigma_{\pm}(i\omega_n)$ as a function of the Matsubara frequency ω_n . On all plots, the even (odd) contribution is plotted in blue (orange). All quantities are depicted for different values of the chemical potential: the upper panel corresponds to $\mu = 1\text{eV}$ and an electron doping $\delta = 0\%$, below $\mu = 1.2\text{eV}$, $\delta = 1\%$, then $\mu = 1.34\text{eV}$, $\delta = 9\%$ and finally $\mu = 1.5\text{eV}$, $\delta = 1.6\%$. Results were obtained for $U = 2\text{eV}$, $T = 54\text{K}$.

It yields both the cluster Green's functions $G_{\pm}^{(n)}$ and self-energies $\Sigma_{\pm}^{(n)}$. The self-consistency condition is used to construct a local diagonal lattice Green's function

$$\hat{G}_{\text{loc},\pm}^{(n)}(i\omega_n) = \sum_{\mathbf{k} \in \text{RBZ}} \left\{ (i\omega_n + \mu) \mathbf{1} - H_{\pm}^{\text{eff}}(\mathbf{k}) - \hat{\Sigma}_{\pm}^{(n)}(i\omega_n) \right\}^{-1}. \quad (\text{C6})$$

This allows to get a new expression for the non-interacting cluster Green's function, via a modified Dyson equation:

$$\left[G_{0,\pm}^{(n+1)} \right]^{-1} = \left[G_{\text{loc},\pm}^{(n)} \right]^{-1} + \Sigma_{\pm}^{(n)}. \quad (\text{C7})$$

This procedure is iterated until convergence.

Appendix D: Absence of a Mott insulator with the standard periodization scheme

The usual periodization of the self-energy writes

$$\tilde{\Sigma}^{\text{latt}}(i\omega_n, \mathbf{k}) = \begin{pmatrix} \Sigma_{AA} & \Sigma_{AB} \times f(\mathbf{k}) \\ \Sigma_{AB} \times f^*(\mathbf{k}) & \Sigma_{AA} \end{pmatrix}, \quad (\text{D1})$$

where

$$f(\mathbf{k}) = \frac{1}{4} \left(1 + e^{-ik_x} + e^{-ik_y} + e^{-i(k_x+k_y)} \right) \quad (\text{D2a})$$

$$= \cos \frac{k_x}{2} \cos \frac{k_y}{2} e^{-i \frac{k_x+k_y}{2}}. \quad (\text{D2b})$$

$\mathbf{k} = (k_1, k_2)$ is expressed in the reduced Brillouin zone. We see from Fig. 2 that the degeneracy of the $(\pi/2, \pi/2) - (\pi, 0)$ path in the full Brillouin zone has to be lifted in order to create a Mott insulating gap. However $f(\mathbf{k}) = 0$ along this path and the self-energy has the following expression

$$\tilde{\Sigma}^{\text{latt}}(i\omega_n, \mathbf{k}) = \Sigma_{AA} \times \mathbf{1}_{2 \times 2}. \quad (\text{D3})$$

Hence the self-energy only renormalizes the chemical potential in the quasiparticle equation (Eq. (20)) at $\omega = 0$, forbidding any lifting of the degeneracy between the quasiparticle bands and therefore any gap in the band structure.

¹ J. J. Randall, L. Katz, and R. Ward, Journal of the American Chemical Society **79**, 266 (1957), <http://dx.doi.org/10.1021/ja01559a004>.

² B. J. Kim, H. Jin, S. J. Moon, J.-Y. Kim, B.-G. Park, C. S. Leem, J. Yu, T. W. Noh, C. Kim, S.-J. Oh, J.-H. Park, V. Durairaj, G. Cao, and E. Rotenberg, Phys. Rev. Lett. **101**, 076402 (2008).

³ C. Martins, M. Aichhorn, L. Vaugier, and S. Biermann, Phys.

Rev. Lett. **107**, 266404 (2011).

⁴ J. Kim, D. Casa, M. H. Upton, T. Gog, Y.-J. Kim, J. F. Mitchell, M. van Veenendaal, M. Daghofer, J. van den Brink, G. Khaliullin, and B. J. Kim, Phys. Rev. Lett. **108**, 177003 (2012).

⁵ A. de la Torre, S. McKeown Walker, F. Y. Bruno, S. Ricc\o, Z. Wang, I. Gutierrez Lezama, G. Scheerer, G. Girit, D. Jaccard, C. Berthod, T. K. Kim, M. Hoesch, E. C. Hunter, R. S.

- Perry, A. Tamai, and F. Baumberger, *Phys. Rev. Lett.* **115**, 176402 (2015).
- ⁶ V. Brouet, J. Mansart, L. Perfetti, C. Piovera, I. Vobornik, P. Le Fèvre, F. m. c. Bertran, S. C. Riggs, M. C. Shapiro, P. Giraldo-Gallo, and I. R. Fisher, *Phys. Rev. B* **92**, 081117 (2015).
- ⁷ K. Terashima, M. Sunagawa, H. Fujiwara, T. Fukura, M. Fujii, K. Okada, K. Horigane, K. Kobayashi, R. Horie, J. Akimitsu, E. Golias, D. Marchenko, A. Varykhalov, N. L. Saini, T. Wakita, Y. Muraoka, and T. Yokoya, *Phys. Rev. B* **96**, 041106 (2017).
- ⁸ J. Nichols, N. Bray-Ali, A. Ansary, G. Cao, and K.-W. Ng, *Phys. Rev. B* **89**, 085125 (2014).
- ⁹ H. Zhang, K. Haule, and D. Vanderbilt, *Phys. Rev. Lett.* **111**, 246402 (2013).
- ¹⁰ H. Watanabe, T. Shirakawa, and S. Yunoki, *Phys. Rev. Lett.* **110**, 027002 (2013).
- ¹¹ Y. Yang, W.-S. Wang, J.-G. Liu, H. Chen, J.-H. Dai, and Q.-H. Wang, *Phys. Rev. B* **89**, 094518 (2014).
- ¹² Y. K. Kim, N. H. Sung, J. D. Denlinger, and B. J. Kim, *Nature Physics* **12**, 37 (2015).
- ¹³ Y. J. Yan, M. Q. Ren, H. C. Xu, B. P. Xie, R. Tao, H. Y. Choi, N. Lee, Y. J. Choi, T. Zhang, and D. L. Feng, *Phys. Rev. X* **5**, 041018 (2015).
- ¹⁴ M. K. Crawford, M. A. Subramanian, R. L. Harlow, J. A. Fernandez-Baca, Z. R. Wang, and D. C. Johnston, *Phys. Rev. B* **49**, 9198 (1994).
- ¹⁵ T. Vogt and D. Buttrey, *Journal of Solid State Chemistry* **123**, 186 (1996).
- ¹⁶ D. J. Singh, P. Blaha, K. Schwarz, and J. O. Sofo, *Phys. Rev. B* **65**, 155109 (2002).
- ¹⁷ K. Rossmagel and N. V. Smith, *Phys. Rev. B* **73**, 073106 (2006).
- ¹⁸ H. J. Xiang and M.-H. Whangbo, *Phys. Rev. B* **75**, 052407 (2007).
- ¹⁹ Y. K. Kim, O. Krupin, J. D. Denlinger, A. Bostwick, E. Rotenberg, Q. Zhao, J. F. Mitchell, J. W. Allen, and B. J. Kim, *Science* **345**, 187 (2014), <http://science.sciencemag.org/content/345/6193/187.full.pdf>.
- ²⁰ A. Hampel, C. Piefke, and F. Lechermann, *Phys. Rev. B* **92**, 085141 (2015).
- ²¹ H. Jin, H. Jeong, T. Ozaki, and J. Yu, *Phys. Rev. B* **80**, 075112 (2009).
- ²² J.-M. Carter, V. Shankar V., and H.-Y. Kee, *Phys. Rev. B* **88**, 035111 (2013).
- ²³ H. Watanabe, T. Shirakawa, and S. Yunoki, *Phys. Rev. Lett.* **105**, 216410 (2010).
- ²⁴ G. Kotliar, S. Y. Savrasov, G. Pálsson, and G. Biroli, *Phys. Rev. Lett.* **87**, 186401 (2001).
- ²⁵ A. Georges, G. Kotliar, W. Krauth, and M. J. Rozenberg, *Rev. Mod. Phys.* **68**, 13 (1996).
- ²⁶ P. Seth, I. Krivenko, M. Ferrero, and O. Parcollet, *Computer Physics Communications* **200**, 274 (2016).
- ²⁷ P. Werner, A. Comanac, L. de' Medici, M. Troyer, and A. J. Millis, *Phys. Rev. Lett.* **97**, 076405 (2006).
- ²⁸ P. Werner and A. J. Millis, *Phys. Rev. B* **74**, 155107 (2006).
- ²⁹ E. Gull, A. J. Millis, A. I. Lichtenstein, A. N. Rubtsov, M. Troyer, and P. Werner, *Rev. Mod. Phys.* **83**, 349 (2011).
- ³⁰ O. Parcollet, M. Ferrero, T. Ayrál, H. Hafermann, I. Krivenko, L. Messio, and P. Seth, *Computer Physics Communications* **196**, 398 (2015).
- ³¹ H. J. Vidberg and J. W. Serene, *J. Low Temp. Phys.* **29**, 179 (1977).
- ³² O. Gunnarsson, T. Schäfer, J. P. F. LeBlanc, E. Gull, J. Merino, G. Sangiovanni, G. Rohringer, and A. Toschi, *Phys. Rev. Lett.* **114**, 236402 (2015).
- ³³ W. Wu, M. Ferrero, A. Georges, and E. Kozik, *Phys. Rev. B* **96**, 041105 (2017).